

# Water cavitation results from the kinetic competition of bulk, surface and surface-defect nucleation events

Philip Loche<sup>a,b</sup>, Matej Kanduč<sup>c</sup>, Emanuel Schneck<sup>d</sup>, and Roland R. Netz<sup>b,1</sup>

<sup>a</sup>Laboratory of Computational Science and Modeling, IMX, École Polytechnique Fédérale de Lausanne, 1015 Lausanne, Switzerland; <sup>b</sup>Fachbereich Physik, Freie Universität Berlin, 14195 Berlin, Germany; <sup>c</sup>Department of Theoretical Physics, Jožef Stefan Institute, 1000 Ljubljana, Slovenia; <sup>d</sup>Physics Department, Technische Universität Darmstadt, 64289 Darmstadt, Germany

This manuscript was compiled on October 24, 2024

**Water at negative pressures can remain in a metastable state for a surprisingly long time before it reaches equilibrium by cavitation, i.e. by the formation of vapor bubbles. The wide spread of experimentally measured cavitation pressures depending on water purity, surface contact angle and surface quality implicates the relevance of water cavitation in bulk, at surfaces and at surface defects for different systems. We formulate a kinetic model that includes all three different cavitation pathways and determine the needed nucleation attempt frequencies in bulk, at surfaces and at defects from atomistic molecular dynamics simulations. Our model reveals that cavitation occurs in pure bulk water only for defect-free hydrophilic surfaces with wetting contact angles below  $50^\circ$  to  $60^\circ$  and at pressures of the order of  $-100$  MPa, depending only slightly on system size and observation time. Cavitation on defect-free surfaces occurs only for higher contact angles, with the typical cavitation pressure rising to about  $-30$  MPa for very hydrophobic surfaces. Nanoscopic hydrophobic surface defects act as very efficient cavitation nuclei and can dominate the cavitation kinetics in a macroscopic system. In fact, a nanoscopic defect that hosts a pre-existing vapor bubble can raise the critical cavitation pressure much further. Our results explain the wide variation of experimentally observed cavitation pressures in synthetic and biological systems and highlight the importance of surface and defect mechanisms for the nucleation of metastable systems.**

cavitation | bubble nucleation | contact angle | molecular dynamics simulation

When water is brought into a metastable state by either heating or pressure reduction, it will eventually reach equilibrium by cavitation, i.e., by the nucleation of vapor bubbles. Cavitation and the collapse of cavitation bubbles are central to applications such as inkjet printing, ultrasonic cleaning, noninvasive destruction of kidney stones by acoustic shockwaves, sonochemistry and sonoluminescence (1, 2). In contrast, the collapse of hydrodynamically produced cavitation bubbles has adverse effects on hydraulic systems, valves and propeller blades, where it causes wear and erosion (3–5). In biology, where temperature is fixed by the environment, metastable water is primarily produced by pressure reduction. The collapse of these cavitation bubbles provides catapult-like mechanisms in ferns (6) and allows snapping shrimp to stun their prey (7). Conversely, cavitation limits the negative pressure produced by octopus suckers (8) and must be avoided in the ascending sap of tall trees, where significantly negative pressures are encountered, in order to prevent embolies (9). Importantly, metastable water at negative pressures can persist over astonishingly long times and cavitation occurs at experimentally relevant time scales only when the pressure sinks below a threshold cavitation pressure  $p_{\text{cav}}$ , which can be as low as

## Significance Statement

Formation of vapor bubbles in heated or depressurized liquid water by cavitation is central for many industrial and biological processes such as inkjet printing, ultrasonic cleaning and sap transport in trees. Where and how bubbles form has remained unclear. By combining molecular simulations with theory, we demonstrate that at negative pressures bubbles form easily at defect-free surfaces if they are not too hydrophilic. A single nanometer-sized hydrophobic surface defect acts as a nucleation site for cavitation and dominates cavitation even in macroscopic systems and at weakly negative pressures. Since defects are inevitable on macroscopic surfaces, this explains why achieving strongly negative pressures in water is difficult and highlights the impact of surfaces and nanodefects on water cavitation.

Author affiliations: <sup>a</sup>Laboratory of Computational Science and Modeling, IMX, École Polytechnique Fédérale de Lausanne, 1015 Lausanne, Switzerland; <sup>b</sup>Fachbereich Physik, Freie Universität Berlin, 14195 Berlin, Germany; <sup>c</sup>Department of Theoretical Physics, Jožef Stefan Institute, 1000 Ljubljana, Slovenia; <sup>d</sup>Physics Department, Technische Universität Darmstadt, 64289 Darmstadt, Germany

P.L. performed the simulations and the analysis. All authors designed the research and wrote the manuscript.

The authors declare no competing interests.

<sup>1</sup>To whom correspondence should be addressed. E-mail: rnetz@physik.fu-berlin.de

–100 MPa in certain systems (2). The large variation of  $p_{\text{cav}}$  among different systems and its dependence on surface properties suggests that cavitation in bulk water (i.e. homogeneous nucleation) competes with cavitation on surfaces (i.e. heterogeneous nucleation) and with cavitation at surface defects. Understanding the kinetic competition between these three different cavitation pathways is important for all the above-mentioned applications and is the central theme of this paper.

Cavitation is a typical nucleation phenomenon; according to Classical Nucleation Theory (CNT), its kinetics is determined by the thermally activated stochastic crossing of a free energy barrier characteristic of the critical nucleus size (10). CNT predicts that clean water at room temperature can sustain negative pressures considerably below –100 MPa before bulk cavitation sets in (2, 11–14). This very low cavitation pressure predicted for clean bulk water is largely due to the high water surface tension. Experimentally, cavitation pressures below –100 MPa have only been reached with ultra-clean water in microscopic quartz cavities (15–17). In typical experiments with hydrophilic surfaces and using rigorous purification and degassing methods, cavitation pressures of the order of  $p_{\text{cav}} \approx -30$  MPa (2, 13, 18) are reached, significantly above the CNT results for clean bulk water. However, with untreated ordinary water in standard containers, the cavitation pressure is positive and typically only slightly below the saturated water vapor pressure of about 2 kPa. The consensus in the field is that surface cavitation at container walls, microscopic impurities (19–25), surface imperfections, or crevices hosting pre-existing vapor or gas bubbles (26–28) contribute to deviations in cavitation pressures from those predicted by CNT for clean bulk water (25, 29). However, a unified theory that accounts for the simultaneous cavitation in bulk water, at surfaces and at surface defects is missing and is formulated in this paper.

Our kinetic cavitation model predicts the cavitation pressure  $p_{\text{cav}}$  as a function of observation time and container size made of surfaces with varying water contact angles and defects with different size and wetting properties. We find that only for very hydrophilic and defect-free surfaces cavitation occurs in bulk and at a cavitation pressure  $p_{\text{cav}}$  given by bulk CNT theory. For defect-free surfaces and above a critical surface contact angle  $\theta$  between  $50^\circ$  and  $60^\circ$  (depending on systems size and observation time), cavitation instead predominantly starts at the surface. Finally, for surfaces that contain defects that are more hydrophobic than the surface, cavitation proceeds from one of the defects with a rate that depends only weakly on the number or surface concentration of defects. For the quantitative comparison of bulk, surface and defect cavitation kinetics we determine their attempt frequencies from all-atom force-field molecular dynamics (MD) simulations, which in the past have proven useful for the study of cavitation processes (25, 30–33).

## Results and Discussion

**A. Kinetic model for cavitation in water confined by surfaces with defects.** In the typical cavitation scenario, water is confined by solid surfaces with a given contact angle that contain a finite number of surface defects. Upon application of a negative pressure, cavitation can proceed in bulk, at the defect-free surface parts or at the defects. Since we cannot presuppose the prevalence of one cavitation pathway over the others, we

write down the total cavitation rate as the sum of the bulk (3D), surface (2D) and defect (def) rates as

$$k_{\text{tot}} = k_{3\text{D}} + k_{2\text{D}} + N_{\text{def}} k_{\text{def}}, \quad [1]$$

where  $N_{\text{def}}$  is the number of surface defects. The model assumes that the different cavitation pathways do not interfere with each other, which we confirm by our MD simulations. It will turn out that depending on the surface and defect properties, quantified by their respective contact angles, one cavitation pathway will always dominate strongly over the other pathways, such that we can construct effective kinetic phase diagrams that feature regions where bulk, surface or defect cavitation dominates.

**B. Cavitation in bulk.** CNT is a general framework for the description of cavitation (10). For cavitation in bulk, one considers a spherical bubble in a liquid with a free energy given by (2, 14, 34)

$$G_{3\text{D}} = 4\pi r^2 \gamma + \frac{4}{3} \pi r^3 p, \quad [2]$$

where  $\gamma$  is the liquid–vapor surface tension,  $r$  the bubble radius and  $p < 0$  the negative pressure in the liquid. The first term represents the bubble surface free energy and the second term the work associated with the volume expansion. We have neglected the saturated vapor pressure, which is irrelevant compared to the large magnitude of cavitation pressures considered here. For simplicity, we have also neglected curvature effects on the surface tension, which only introduce minor corrections (30, 35). The interplay between the two terms in Eq. 2 creates a free energy barrier for  $p < 0$  of

$$G_{3\text{D}}^* = \frac{16\pi}{3} \frac{\gamma^3}{p^2}, \quad [3]$$

reached at the critical bubble radius  $r^* = -2\gamma/p$  defined by  $dG_{3\text{D}}/dr|_{r=r^*} = 0$ . If a bubble surpasses the critical radius  $r^*$ , it will grow further and cause cavitation.

Cavitation can occur anywhere in bulk, its rate therefore is proportional to the liquid volume  $V$  and can be written as

$$k_{3\text{D}} = \kappa_{3\text{D}} V e^{-\beta G_{3\text{D}}^*}. \quad [4]$$

The cavitation time follows from the rate as  $\tau = k_{3\text{D}}^{-1}$  (36) and is the mean time one has to wait for cavitation to occur. The exponential factor in Eq. 4 reflects the Arrhenius law (36), where  $\beta = 1/k_{\text{B}}T$  is the inverse thermal energy. The pre-exponential factor splits into the volume  $V$  and the attempt frequency density  $\kappa_{3\text{D}}$ , which is an intensive property of the liquid that characterizes the barrier-less cavitation rate. It thus constitutes the cavitation speed limit, i.e., the maximum rate at which cavitation can occur (37). The attempt frequency density,  $\kappa_{3\text{D}}$ , accounts for viscosity and hydrodynamic memory effects in the surrounding liquid, as well as for corrections to CNT, such as the curvature dependence of the interfacial tension (38). Given the exponential dependence of the cavitation time  $\tau$  on  $p$ , it is preferred to consider the inverse relation. For a cubic volume  $V = L^3$ , the cavitation pressure follows from Eqs. 3 and 4 as (2, 39)

$$p_{3\text{Dcav}}^2 = \frac{16\pi\gamma^3}{3k_{\text{B}}T} \frac{1}{\ln(\kappa_{3\text{D}} L^3 \tau)}. \quad [5]$$

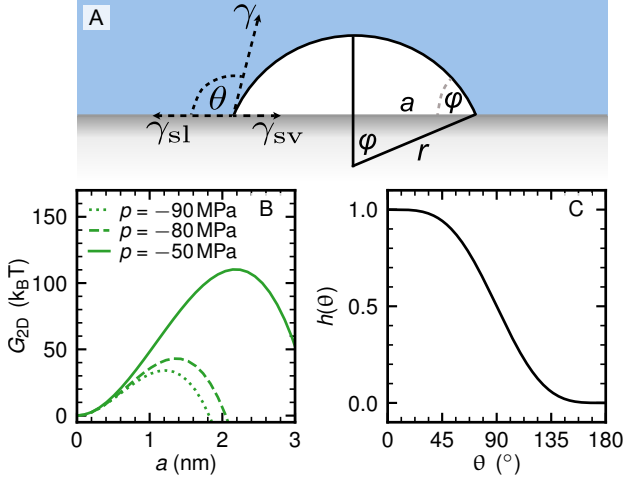


**Fig. 1.** (A) Schematics of bubble cavitation on a surface. Bubble contact angle  $\varphi$  and water contact angle  $\theta$  are related by  $\varphi = \pi - \theta$ . (B) Free energy  $G_{2D}$  of a bubble on a surface with a contact angle of  $\theta = 97^\circ$  as a function of the bubble base radius  $a$  from Eq. 6 for various negative pressures  $p$ . (C) Geometric factor  $h(\theta) = G_{2D}^*/G_{3D}^*$  in Eq. 8.

It is seen that  $p_{3Dcav}$  depends only logarithmically and thus rather weakly on system size  $L$  and cavitation time  $\tau$ . Various methods to determine  $\kappa_{3D}$  exist (40, 41). Here, we use the value of  $\kappa_{3D}$  from our previous MD simulations (35), which will allow us to compare with surface-cavitation and defect-cavitation rates obtained by the same method on the same footing. In our previous simulation study on bulk cavitation, we determined  $\kappa_{3D} = 5 \times 10^{11} \text{ ns}^{-1} \text{ nm}^{-3}$  for the SPC/E water model (35), yielding  $p_{3Dcav}$  between  $-80$  and  $-100$  MPa for  $L$  between  $1 \mu\text{m}$  and  $1 \text{ m}$  and  $\tau = 1 \text{ s}$  according to Eq. 5. This value is slightly lower than previous predictions, primarily because the surface tension of SPC/E water ( $\gamma_{SPC/E} \approx 55 \text{ mN/m}$  for a Lennard-Jones cutoff  $0.9 \text{ nm}$  (42)) is lower than the experimental value  $\gamma_{exp} = 72 \text{ mN/m}$ . Applying a correction factor of  $(\gamma_{exp}/\gamma_{SPC/E})^{3/2} \approx 1.5$  on  $p_{3Dcav}$ , as suggested by Eq. 5, yields good agreement with previous predictions (2, 11–14). We here stick to the SCP/E water model because it reproduces most dynamic water properties quite well.

**C. Cavitation at a smooth defect-free surface.** To apply the CNT framework, we write the free energy of a bubble at a surface, illustrated in Fig. 1 A, as

$$G_{2D} = A_{cap}\gamma + A_{base}(\gamma_{sv} - \gamma_{sl}) + pV_b, \quad [6]$$

where  $A_{cap} = 2\pi r^2(1 - \cos \varphi)$  is the area of the spherical bubble cap with radius of curvature  $r$ ,  $A_{base} = \pi a^2$  is the base area of the bubble with base radius  $a$  and  $V_b = (\pi/3)r^3(2 - 3\cos \varphi + \cos^3 \varphi)$  is the bubble volume,  $\gamma_{sv}$  and  $\gamma_{sl}$  correspond to the solid–vapor and solid–liquid surface tensions, respectively, and  $\varphi$  is the contact angle of the bubble. Similar to Eq. 2, the first two terms account for the free energy of creating the bubble surface and the third term is the work associated with volume expansion. We neglect the buoyancy force, as it is irrelevant for determining the critical bubble size, which is on the nanometer scale, and mostly important for the pinching-off of full-grown bubbles.

Using Young’s equation,  $\gamma_{sv} - \gamma_{sl} = \gamma \cos \theta$ , and the relation between the water contact angle  $\theta$  and the bubble contact

angle  $\varphi$ ,  $\varphi + \theta = 180^\circ$ , we show in Fig. 1 B the free energy of a bubble at a hydrophobic surface characterized by a water contact angle  $\theta = 97^\circ$  according to Eq. 6 as a function of the base radius  $a$  for various pressures. The critical bubble size follows from  $dG_{2D}/da|_{a=a^*} = 0$  as  $a^* = -(2\gamma/p) \sin \theta$ , the corresponding radius of curvature is  $r^* = -2\gamma/p$ , as for homogeneous cavitation. The free energy barrier follows as

$$G_{2D}^*(\theta) = G_{3D}^* h(\theta), \quad [7]$$

which is reduced compared to the bulk result  $G_{3D}^*$  in Eq. 3 by the geometric factor (2, 10, 21, 43)

$$h(\theta) = (2 - \cos \theta) \cos^4(\theta/2) \quad [8]$$

depicted in Fig. 1 C. For a completely wetting surface,  $\theta = 0$ , we find  $h(0) = 1$ , the bubble is detached from the surface and the bulk cavitation result is recovered. The factor  $h(\theta)$  decreases as the contact angle increases, ultimately disappearing for  $\theta = 180^\circ$ . The surface cavitation rate is written as

$$k_{2D} = A\kappa_{2D}(\theta) e^{-\beta G_{2D}^*(\theta)} \quad [9]$$

and is proportional to the total surface area  $A$ , where  $\kappa_{2D}$  is the attempt frequency surface density, which depends on the surface type and thus on the contact angle  $\theta$ . For the total surface area of a cubic container  $A = 6L^2$  and neglecting edge and corner effects, the surface cavitation pressure is given by

$$p_{2Dcav}^2 = \frac{16\pi\gamma^3}{3k_B T} \frac{h(\theta)}{\ln[\kappa_{2D}(\theta) 6L^2 \tau]}. \quad [10]$$

To determine  $\kappa_{2D}$  from simulations, we use a self-assembled monolayer of alkyl molecules terminated by headgroups with adjustable electric dipole moments (42, 44). The dipole moment controls the wetting characteristics of the surfaces. We examine six different dipole moments, resulting in contact angles of  $45^\circ$ ,  $60^\circ$ ,  $76^\circ$ ,  $97^\circ$ ,  $120^\circ$  and  $135^\circ$ , on surfaces measuring  $9 \text{ nm} \times 10.4 \text{ nm}$  in contact with water. Obtaining the cavitation time from simulations at constant negative pressure is impractical due to the excessive waiting time for cavitation to occur. Instead, we apply negative pressures that decrease linearly over time as  $p(t) = \dot{p}t$  with different fixed pressure ramp rates  $\dot{p} < 0$ , as used before for bulk cavitation (35) and described in the methods section.

Fig. 2 summarizes our simulation results. Panel A illustrates a cavitation event on a hydrophobic surface with contact angle  $\theta = 97^\circ$ , where a vapor bubble forms at the surface (see inset snapshots) due to the progressively decreasing pressure over time (upper graph). The simulation trajectory consists of a sequence of 20-ps-long simulations (delineated by gray vertical lines), each at a constant applied pressure that decreases in discrete steps of  $0.1 \text{ MPa}$ , which corresponds to a mean pressure rate of  $\dot{p} = -5 \text{ MPa/ns}$ . The formation of the bubble is monitored by the box size normal to the surface  $L_z$  (bottom graph). We define cavitation to take place when the box size  $L_z$  increases by 50% compared to its initial value, which in this specific example yields a cavitation pressure  $p_{2Dcav}^* = -93.9 \text{ MPa}$ . It is important to note that the cavitation pressure in the pressure-ramp ensemble  $p_{2Dcav}^*$  is different from the cavitation pressure  $p_{2Dcav}$  in the constant-pressure ensemble given in Eq. 10, which will be determined later.

Representative snapshots of cavitation at surfaces with different contact angles are presented in Fig. 2 B. Fig. 2 C shows

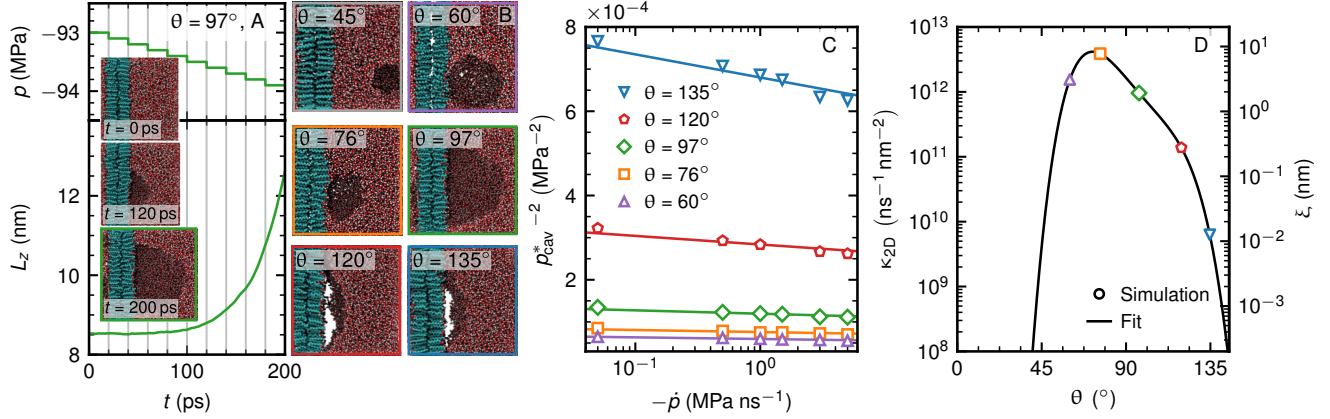


**Fig. 2.** (A) Time-dependent pressure ( $p$ , top) and simulation box size ( $L_z$ , bottom) during a pressure ramp simulation with a pressure rate of  $\dot{p} = -5$  MPa/ns for a system with a surface contact angle of  $\theta = 97^\circ$ . The presented trajectory corresponds to the final 200 ps prior to cavitation, identified as a 50% increase of  $L_z$  relative to its initial value  $L_z^0 = 8$  nm. We find a cavitation pressure of  $p_{\text{cav}}^* = -93.9$  MPa. Vertical lines mark individual simulation segments at constant pressure. The inset shows consecutive snapshots of the cavitation event. (B) Cavitation configurations with  $L_z/L_z^0 = 3/2$  for different contact angles. (C) Simulation results for  $(p_{\text{cav}}^*)^{-2}$  versus  $\dot{p}$  for different contact angles. The lines are fits of Eq. 16 to the data, where  $\kappa_{2D}$  is the only fitting parameter. (D) Results for  $\kappa_{2D}$  (left scale) and the ratio  $\xi = \kappa_{2D}/\kappa_{3D}$  (right scale) as a function of contact angle  $\theta$ . The solid black line is a fit of Eq. S1 in the SI Appendix, section S1.

$1/p_{\text{cav}}^{*2}$  versus the negative pressure-ramp rate  $-\dot{p}$ . Each data point represents an average over 10 independent simulations. The solid lines are fits of the kinetic theory for  $p_{2D\text{cav}}^*$  assuming pure surface cavitation given in Eq. 16, from which the values of  $\kappa_{2D}(\theta)$  for each  $\theta$  are obtained. For the lowest contact angle of  $45^\circ$ , bubble cavitation occurs in the bulk. Therefore, this surface is not included in the analysis in Fig. 2 C. The resulting values for  $\kappa_{2D}$  (symbols) are shown as a function of the surface contact angle  $\theta$  in Fig. 2 D. We also denote the characteristic length  $\xi = \kappa_{2D}/\kappa_{3D}$  by the scale on the right, which represents the water slab height for which the surface cavitation attempt frequency  $\kappa_{2D}$  equals the bulk attempt frequency  $\kappa_{3D}$ . It can be seen that  $\xi$  exhibits a maximum around  $\theta \approx 75^\circ$  and goes dramatically down with increasing contact angle from approximately 10 to  $10^{-2}$  nm. This suggests that a hydrophilic surface produces more cavitation nuclei in a given time than a hydrophobic surface, which is interesting since it contrasts with the pronounced density fluctuations at hydrophobic surfaces (45) (alternatively, it could reflect inaccuracies of the bulk and surface barrier free energy expressions). Clearly, this variation of  $\kappa_{2D}$  is subdominant compared to the variation of the exponential barrier energy in Eq. 9, but nevertheless has to be included for a quantitative comparison of surface and bulk cavitation kinetics. For our subsequent analyses, we fit our simulation data for  $\kappa_{2D}$  in Fig. 2 D to a function shown as a solid line, as detailed in the SI Appendix, section S1.

#### D. Kinetic competition between cavitation in bulk and at a defect-free surface.

In the absence of defects we set  $N_{\text{def}} = 0$  in Eq. 1. The cavitation pressure  $p_{\text{cav}}$  cannot be derived analytically, therefore, we solve Eq. 1 numerically and plot  $p_{\text{cav}}$  in Fig. 3 A (solid lines) against the surface contact angle  $\theta$  for different cube sizes  $L$  and a fixed waiting time of  $\tau = k_{\text{tot}}^{-1} = 1$  s. For hydrophilic surfaces with small  $\theta$ ,  $p_{\text{cav}}$  is dominated by bulk cavitation (thus,  $k_{\text{tot}} \approx k_{3D}$ ) and becomes independent of  $\theta$ , as described by Eq. 5 and represented by the horizontal dashed lines. For larger contact angles  $\theta$  the cavitation pressure is well described by the surface prediction Eq. 10, shown as dotted lines, which indicates that cavitation for large  $\theta$  predominantly

occurs at surfaces.

It is seen that cavitation shifts from the bulk (3D) to the surface (2D) pathway rather abruptly at a well-defined crossover contact angle  $\theta^*$ , which defines the onset of surface cavitation. Thus,  $\theta^*$  is identified as the intersection of the bulk prediction (dashed lines) and the surface prediction (dotted lines) in Fig. 3 A. In SI Appendix, section S2, we present results for a range of different waiting times  $\tau$  from  $10^{-3}$  to  $10^3$  s, showing the same sharp transition between the surface-dominated and the bulk-dominated regimes. By equating Eq. 5 and Eq. 10 we obtain an exact expression for the critical system size  $L^*$  at which the transition takes place

$$L^* = [6\tau\kappa_{2D}(\theta)(\kappa_{3D}\tau)^{-h(\theta)}]^{1/[3h(\theta)-2]}, \quad [11]$$

whose inverse (i.e.,  $\theta^*$  as a function of  $L$ ) is presented in Fig. 3 B for various cavitation times  $\tau$ . It transpires that  $\theta^*$  varies within a narrow window between  $50^\circ$  and  $60^\circ$  for order-of-magnitude variations of system size  $L$  and cavitation time  $\tau$ .

This weak dependence of  $\theta^*$  on  $L$  and  $\tau$  can be understood from the analytical inverse of Eq. 11 valid for small  $\theta$ ,

$$\theta^* \approx \left\{ \frac{16 \ln[L/(6\xi)]}{3 \ln(\kappa_{3D}L^3\tau)} \right\}^{1/4}, \quad [12]$$

see SI Appendix, section S3 for the derivation. The critical contact angle depends as a quartic square root on the logarithm of  $L$  and  $\tau$ , which is an extremely weakly varying function.

We conclude that surface cavitation occurs if the contact angle of the confining surfaces exceeds the threshold value  $\theta^*$ , which is largely independent of system size and waiting time. Although surfaces with contact angles below the threshold, i.e. for  $\theta < \theta^*$ , do have a lower cavitation free energy barrier compared to bulk cavitation, as predicted by Eq. 7, they exhibit a smaller cavitation rate due to the different attempt frequencies at a surface and in bulk, as quantified by the length scale  $\xi$ . This renders surface cavitation on hydrophilic surfaces less likely than bulk cavitation.

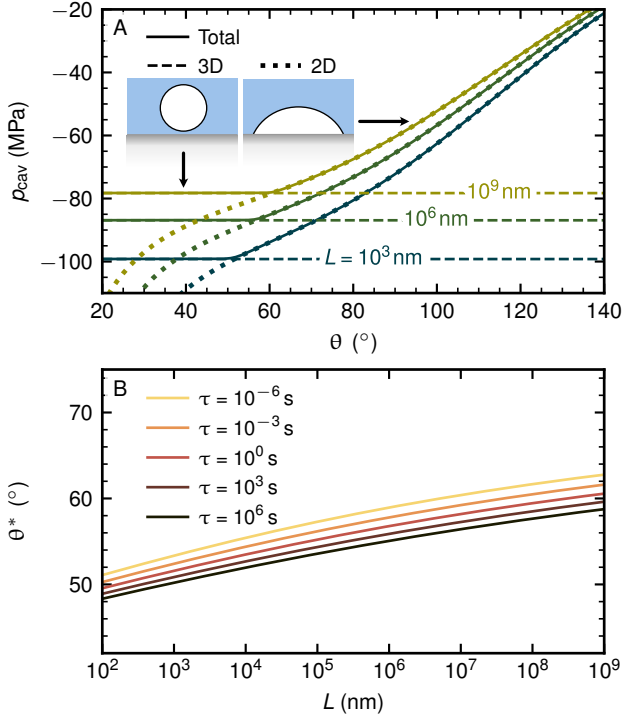


**Fig. 3.** (A) Cavitation pressure  $p_{cav}$  of a water-filled cubic container as a function of the contact angle  $\theta$  of the defect-free inner walls, for a fixed waiting time of  $\tau = 1$  s, computed by numerically inverting Eq. 1 for  $N_{def} = 0$  (solid lines). Different colors represent different cube sizes  $L$ . Dotted lines show the 2D cavitation pressure according to Eq. 10, while dashed lines denote the 3D cavitation pressure based on Eq. 5. (B) Crossover contact angle  $\theta^*$ , where  $k_{2D} = k_{3D}$ , as a function of container size  $L$  for different waiting times  $\tau$ , according to Eq. 11.

**E. Cavitation at surface defects.** Real-world surfaces are rich in surface defects such as vacancies, disordered regions, variations in material composition and adsorbed organic or inorganic species (46). We model defects as circular patches with radius  $R_{def}$  and contact angle  $\theta_{def}$ , as illustrated in Fig. 4 A. We assume the defects to be larger than the critical bubble base radius  $a^*$  and much smaller than the system size  $L$ ,  $a^* \ll R_{def} \ll L$ . With these assumptions, the single defect cavitation rate in Eq. 1 is given in analogy to Eq. 9 as

$$k_{def} = \kappa_{2D}(\theta_{def}) A_{def} e^{-\beta G_{2D}^*(\theta_{def})}, \quad [13]$$

with the defect surface area given by  $A_{def} = \pi R_{def}^2$  and the attempt frequency density  $\kappa_{2D}$  and the free energy barrier  $G_{2D}^*$  determined by the defect contact angle  $\theta_{def}$ . The defect cavitation pressure follows from Eq. 13 by using Eq. 7 and  $\tau = 1/(N_{def} k_{def})$  as

$$p_{defcav}^2 = \frac{16\pi\gamma^3}{3k_B T} \frac{h(\theta_{def})}{\ln[\kappa_{2D}(\theta_{def}) \pi R_{def}^2 \tau N_{def}]}. \quad [14]$$

The total cavitation rate in Eq. 1 describes the kinetic competition between cavitation in bulk, at surfaces and at defects. The cavitation pressure resulting from this competition is determined by solving Eq. 1 in conjunction with Eqs. 4, 9, 13 for a given set of parameters  $L$ ,  $\tau$ ,  $\theta$ ,  $N_{def}$  and  $\theta_{def}$ .

For the following discussion, we assume that the surface is sufficiently hydrophilic so that  $k_{2D} \ll k_{3D}$  and cavitation at the defect-free surface parts can be neglected. The solid

lines in Fig. 4B show the cavitation pressure in a 1 mL cube of water ( $L = 1$  cm) in the presence of a single surface defect,  $N_{def} = 1$ , as a function of the defect radius  $R_{def}$  for different defect contact angles  $\theta_{def}$ . For a given  $\theta_{def}$  a well-defined crossover radius  $R_{def}^*$  emerges, at which the system transitions from bulk cavitation for small  $R_{def}$ , where the bulk prediction Eq. 5 (dashed line) is valid, to defect cavitation for large  $R_{def}$ , where the prediction in Eq. 14 (dotted lines) is valid. The crossover radius  $R_{def}^*$  grows as  $\theta_{def}$  approaches  $\theta^*$  from above. Conversely, for increasing  $\theta_{def}$  the crossover radius  $R_{def}^*$  approaches sub-nanometer values (where our continuum model will eventually break down). The results in Fig. 4B show that cavitation is dominated by defects with a radius larger than a critical value  $R_{def}^*$  and occurs at a rate  $N_{def} k_{def}$ ; even a single hydrophobic defect can dominate the cavitation kinetics in macroscopic systems.

The crossover radius  $R_{def}^*$  between the cavitation pressures for the bulk and defect pathways follows from equating Eqs. 5 and 14 as

$$R_{def}^{*2} = \frac{(\kappa_{3D} L^3 \tau)^{h(\theta_{def})}}{\pi \kappa_{2D}(\theta_{def}) \tau N_{def}}. \quad [15]$$

In Fig. 4 C we show  $R_{def}^*$  as a function of system size  $L$  for a waiting time  $\tau = 1$  s and a single defect  $N_{def} = 1$  for three different defect contact angles. As the system size increases, a larger defect is required to induce defect cavitation. Conversely, for larger defect contact angle  $\theta_{def}$  the crossover radius  $R_{def}^*$  decreases and reaches a nanometer even for macroscopically large systems. For a surface with many defects,  $N_{def} > 1$ , the required defect radius  $R_{def}^*$  is from Eq. 15 predicted to go further down.

Finally, we check our theoretical predictions by explicit simulations of a system featuring one defect. We choose a mildly hydrophobic surface with a contact angle of  $\theta = 97^\circ$  on which we create one circular defect by removing surface molecules within a radius of  $R_{def}$  on one monolayer, thereby forming a hydrophobic pit with a depth of 1 nm. Water does not enter the pit because of its hydrophobic interior, creating a vapor bubble, corresponding to a defect contact angle of  $\theta_{def} \approx 180^\circ$ . To avoid cavitation at the opposite monolayer, we make it hydrophilic with a contact angle of  $42^\circ$ . Using the pressure ramp protocol, we consistently observe bubble formation at the hydrophobic pit, as shown in Fig. 4 D, despite the rest of the surface being mildly hydrophobic. Using a pressure rate of  $\dot{p} = -5$  MPa/ns, a defect-free surface induces surface cavitation at  $p_{cav}^* = -95 \pm 1$  MPa, as seen in Fig. 2 C. In contrast, the systems with surface defects of 1 and 2 nm radii cavitate already at  $p_{cav}^* = -66$  and  $-45 \pm 2$  MPa, respectively, in qualitative agreement with our predictions in Fig. 4 B.

## Conclusion

By combining MD simulations with CNT analysis, we explore the kinetic competition between bulk, surface and defect cavitation of water under negative pressure. For defect-free surfaces, the prevalent cavitation pathway shifts abruptly from bulk to surface when the surface contact angle increases above a threshold in the range  $\theta^* \approx 50^\circ$  to  $60^\circ$ , depending slightly on system size and waiting time. The typical cavitation pressure decreases in magnitude from about  $p_{cav} \approx -100$  MPa for bulk to about  $p_{cav} \approx -30$  MPa for hydrophobic surface cavitation. Even the presence of a single nanoscopic hydrophobic

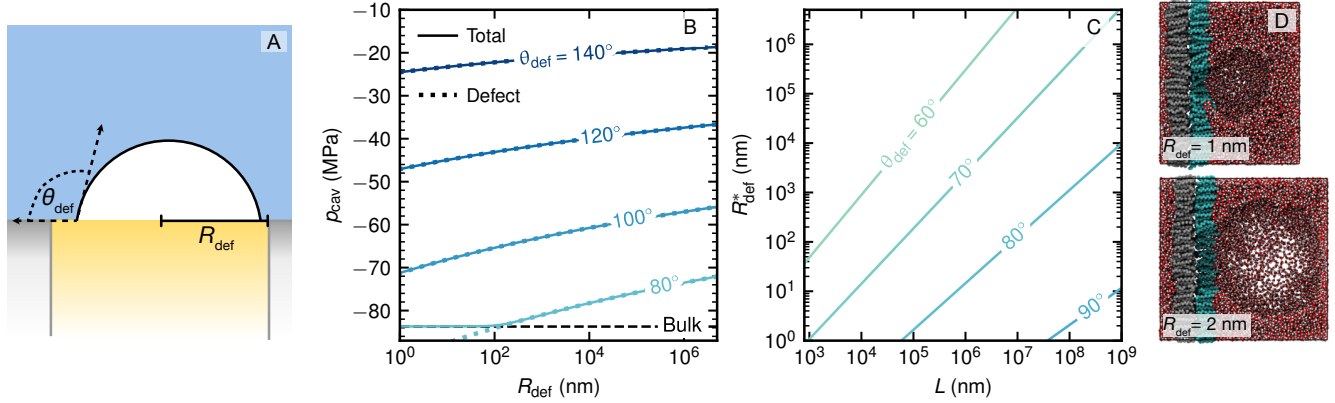


**Fig. 4.** (A) Illustration of a cavitation bubble on a circular surface defect with radius  $R_{\text{def}}$  and contact angle  $\theta_{\text{def}}$  on a flat surface of contact angle  $\theta$ . (B) Cavitation pressure of a water-filled container with a single surface defect  $N_{\text{def}} = 1$  as a function of  $R_{\text{def}}$  for different  $\theta_{\text{def}}$ . Solid lines are obtained by numerically solving Eq. 1 for a waiting time of  $\tau = 1$  s and a container size of  $L = 1$  cm (volume of 1 mL). Dotted lines show the limiting pressure for a large defect, given by Eq. 14, whereas the dashed line shows the bulk cavitation pressure Eq. 5. (C) Crossover defect radius as a function of container size  $L$  for a fixed waiting time of  $\tau = 1$  s from Eq. 15. (D) Simulation snapshots for box expansions of  $L_z/L_{z0} = 3/2$  after cavitation in systems with a surface contact angle of  $97^\circ$  and cylindrical hydrophobic pits, from pressure-ramp simulations at a rate of  $\dot{p} = -5$  MPa/ns. The pits have radii of  $R_{\text{def}} \approx 1$  nm and 2 nm.

surface defect dominates the cavitation kinetics and substantially raises the cavitation pressure values, depending on the defect contact angle and defect size. Since even with the most advanced fabrication techniques surface defects are unavoidable, this explains why experimental cavitation pressures for typical surface materials are far above the predicted value for bulk cavitation and why low cavitation pressures around  $p_{\text{cav}} \approx -100$  MPa are only achieved in micro-sized defect-free quartz cavities (15–17).

In every-day life, water contains a variety of organic and inorganic substances. The bulk–surface cavitation crossover contact angle  $\theta^*$  is close to the ‘Berg limit’ (47–49): Surfaces with larger contact angles are prone to macromolecule adhesion, which tends to make them more hydrophilic (50) and thus can prevent surface cavitation. Such a mechanism might be important for preventing embolies in the sap of tall trees. We have treated negative-pressure-induced cavitation in water at constant temperature. However, our methods can also be used for other liquids and to study cavitation in superheated liquids and nucleation in supersaturated solutions, where we expect surface and defect nucleation to play equally important roles.

## Materials and Methods

**Simulation model.** The simulation setup follows our previous approach (42, 44). We model a planar surface composed of two self-assembled monolayers, each consisting of ten-carbon-atom alkyl chains terminated by polar hydroxyl (OH) head groups. The molecules are arranged on a hexagonal lattice with a density of  $4.3 \text{ nm}^{-2}$ . To stabilize the structure, we apply harmonic restraints to the second carbon atom from the head group with strengths of  $k_x = k_y = 500$  (kJ/mol)  $\text{nm}^{-2}$  in the lateral directions, and to the tenth (terminal) carbon atom with  $k_x = k_y = 10$  (kJ/mol)  $\text{nm}^{-2}$  laterally and  $k_z = 100$  (kJ/mol)  $\text{nm}^{-2}$  in the normal direction. The surface polarity and thereby the surface contact angle is controlled by scaling the partial charges of the head groups with a factor  $\alpha$ , ranging from 0 to 1. For  $\alpha = 0$ , the surface is non-polar with head groups resembling methylated termini, resulting in a contact angle of  $\theta = 135^\circ$ . For  $\alpha = 1$ , the surface is fully polar, mimicking hydroxyl head groups. The relationship between  $\alpha$  and  $\cos\theta$  is discussed in SI Appendix, section S4. The periodic simulation box,

with initial dimensions  $9 \text{ nm} \times 10.4 \text{ nm} \times 8 \text{ nm}$ , contains 16,353 water molecules and 800 hydroxylated alkanes.

We use united-atom parameters from the GROMOS force field for the alkanes (42, 51) and the SPC/E water model (52). Classical non-polarizable molecular dynamics simulations are performed with the GROMACS package (53) using a time step of 2 fs. A plain cutoff of 0.9 nm is used for short-range Lennard-Jones interactions. Electrostatics is treated with the Smooth Particle–Mesh Ewald method, using a 0.9 nm real-space cutoff. A temperature of 300 K is controlled using the velocity rescale thermostat with a stochastic factor (54) and a time constant of 0.5 ps. Pressure is controlled by the Berendsen barostat with a time constant of 1 ps, suitable even for negative pressures because of its efficiency and stability in box scaling under large pressure differences. We previously verified (35) that equivalent results are obtained with the Parrinello–Rahman barostat, which more accurately reproduces volume fluctuations. Reference coordinates for surface-atom restraints are scaled with the coupling matrix of the pressure coupling.

To simulate pressure ramps, we conduct a sequence of simulations at constant pressures, starting from an initial pressure of  $-30$  MPa. After each simulation, the final coordinates are used to start the next simulation, with the pressure reduced by 0.1 MPa. The duration of each constant-pressure simulation depends on the pressure rate  $\dot{p}$ .

**Kinetic theory for pressure ramps.** To obtain the cavitation attempt frequencies, we use the pressure-ramp simulation protocol (35), where the negative pressure decreases linearly over time as  $p(t) = \dot{p}t$  at a constant rate  $\dot{p} < 0$ . We identify cavitation when the simulation box length  $L_z$  increases by more than 50% of its initial value. The corresponding pressure-ramp cavitation pressure  $p_{\text{cav}}^*$  follows from the solution of the linear cavitation rate-equation as

$$p_{\text{cav}}^* = \dot{p} \int_0^\infty e^{-k_0 I(t)} dt, \quad [16]$$

where

$$I(t) = \int_0^t e^{-\beta G^*(t')} dt'. \quad [17]$$

Here,  $G^*(t)$  is the time-dependent free energy barrier in the pressure ramp protocol which, according to CNT, decay inversely with time as  $G^*(t) \sim t^{-2}$ . The attempt frequencies for bulk and surface cavitation,  $\kappa_{3D}$  and  $\kappa_{2D}$ , are obtained from fits of Eq. 16 to the simulation data; detail are given in SI Appendix, section S5.

**Data, Materials, and Software Availability.** All simulation input files as well as Python functions to fit  $\kappa_{2D}$  and perform further

analysis from the simulations are available [online](#).

**ACKNOWLEDGMENTS.** M.K. acknowledges financial support from the Slovenian Research and Innovation Agency ARIS (contracts P1-0055 and J1-4382).

1. AJ Coleman, JE Saunders, A survey of the acoustic output of commercial extracorporeal shock wave lithotripters. *Ultrasound Med Biol* **15**, 213–227 (1989).
2. F Caupin, E Herbert, Cavitation in water: a review. *Comptes Rendus Physique* **7**, 1000–1017 (2006).
3. M Dular, B Bachert, B Stoffel, B Širok, Relationship between cavitation structures and cavitation damage. *Wear* **257**, 1176–1184 (2004).
4. F Reuter, C Deiter, CD Ohl, Cavitation erosion by shockwave self-focusing of a single bubble. *Ultrason. Sonochem* **90**, 106131 (2022).
5. U Adhikari, A Goliaei, ML Berkowitz, Mechanism of membrane poration by shock wave induced nanobubble collapse: A molecular dynamics study. *J. Phys. Chem. B* **119**, 6225–6234 (2015).
6. X Noblin, et al., The fern sporangium: a unique catapult. *Science* **335**, 1322–1322 (2012).
7. M Verslius, B Schmitz, A von der Heydt, D Lohse, How snapping shrimp snap: Through cavitating bubbles. *Science* **289**, 2114 (2000).
8. AM Smith, Negative pressure generated by octopus suckers: a study of the tensile strength of water in nature. *J. Exp. Biol.* **157**, 257–271 (1991).
9. AD Stroock, VV Pagay, MA Zwieniecki, N Michele Holbrook, The physicochemical hydrodynamics of vascular plants. *Annu. Rev. Fluid Mech.* **46**, 615–642 (2014).
10. PG Debenedetti, *Metastable Liquids: Concepts and Principles*. (Princeton University Press) Vol. 1, (1996).
11. JC Fisher, The Fracture of Liquids. *J. Appl. Phys.* **19**, 1062–1067 (1948).
12. F Caupin, Liquid-vapor interface, cavitation, and the phase diagram of water. *Phys. Rev. E* **71**, 051605 (2005).
13. F Caupin, AD Stroock, The stability limit and other open questions on water at negative pressure. *Liq. Polymorph.* **152**, 51–80 (2013).
14. MEM Azouzi, C Ramboz, JF Lenain, F Caupin, A coherent picture of water at extreme negative pressure. *Nat. Phys.* **9**, 38–41 (2013).
15. Q Zheng, DJ Durben, GH Wolf, C. A. Angell, Liquids at large negative pressures: Water at the homogeneous nucleation limit. *Science* **254**, 829–832 (1991).
16. A Alvarenga, M Grimsditch, R Bodnar, Elastic properties of water under negative pressures. *J. Chem. Phys.* **98**, 8392–8396 (1993).
17. MEM Azouzi, C Ramboz, JF Lenain, F Caupin, A coherent picture of water at extreme negative pressure. *Nat. Phys.* **9**, 38–41 (2013).
18. F Caupin, Escaping the no man's land: Recent experiments on metastable liquid water. *J. Non-Cryst. Solids* **407**, 441–448 (2015).
19. SF Jones, GM Evans, KP Galvin, Bubble nucleation from gas cavities — a review. *Adv. Colloid Interface Sci.* **80**, 27–50 (1999).
20. HB Marschall, KA Mørch, AP Keller, M Kjeldsen, Cavitation inception by almost spherical solid particles in water. *Phys. Fluids* **15**, 545–553 (2003).
21. RP Sear, Nucleation: theory and applications to protein solutions and colloidal suspensions. *J. Condens. Matter Phys.* **19**, 033101 (2007).
22. KA Mørch, Reflections on cavitation nuclei in water. *Phys. Fluids* **19** (2007).
23. Si Tsuda, S Takagi, Y Matsumoto, A study on the growth of cavitation bubble nuclei using large-scale molecular dynamics simulations. *Fluid Dyn. Res.* **40**, 606 (2008).
24. T Groß, P Pelz, Diffusion-driven nucleation from surface nuclei in hydrodynamic cavitation. *J. Fluid Mech.* **830**, 138–164 (2017).
25. Z Gao, W Wu, B Wang, The effects of nanoscale nuclei on cavitation. *J. Fluid Mech.* **911**, A20 (2021).
26. EN Harvey, et al., Bubble formation in animals. I. Physical factors. *J. Cell. Comp. Physiol.* **24**, 1–22 (1944).
27. AA Atchley, A Prosperetti, The crevice model of bubble nucleation. *The J. Acoust. Soc. Am.* **86**, 1065–1084 (1989).
28. P Pfeiffer, et al., Heterogeneous cavitation from atomically smooth liquid–liquid interfaces. *Nat. Phys.* **18**, 1431–1435 (2022).
29. X Zhang, et al., A critical review on challenges and trend of ultrapure water production process. *Sci. Total. Environ.* **785**, 147254 (2021).
30. G Menzl, et al., Molecular mechanism for cavitation in water under tension. *Proc. Natl. Acad. Sci.* **113**, 13582–13587 (2016).
31. Y Zhou, B Li, Y Gu, M Chen, A molecular dynamics simulation study on the cavitation inception of water with dissolved gases. *Mol. Phys.* **117**, 1894–1902 (2019).
32. D Dockar, MK Borg, JM Reese, Mechanical Stability of Surface Nanobubbles. *Langmuir* **35**, 9325–9333 (2019).
33. Y Liu, S Bernardi, A Widmer-Cooper, Stability of pinned surface nanobubbles against expansion: Insights from theory and simulation. *J. Chem. Phys.* **153** (2020).
34. G Menzl, C Dellago, Effect of entropy on the nucleation of cavitation bubbles in water under tension. *J. Chem. Phys.* **145**, 211918 (2016).
35. M Kanduć, et al., Cavitation in lipid bilayers poses strict negative pressure stability limit in biological liquids. *PNAS* **117**, 10733–10739 (2020).
36. P Hänggi, P Talkner, M Borkovec, Reaction-rate theory: fifty years after kramers. *Rev. Mod. Phys.* **62**, 251 (1990).
37. J Kubelka, J Hofrichter, WA Eaton, The protein folding 'speed limit'. *Curr. Opin. Struct. Biol.* **14**, 76 (2004).
38. S Acharya, B Bagchi, Rate theory of gas–liquid nucleation: Quest for the elusive quantitative accuracy. *J. Chem. Phys.* **160**, 174503 (2024).
39. E Herbert, S Balibar, F Caupin, Cavitation pressure in water. *Phys. Rev. E* **74**, 041603 (2006).
40. M Blander, JL Katz, Bubble nucleation in liquids. *AIChE J.* **21**, 833–848 (1975).
41. M Pettersen, S Balibar, H Maris, Experimental investigation of cavitation in superfluid He 4. *Phys. Rev. B* **49**, 12062 (1994).
42. M Kanduć, RR Netz, Atomistic simulations of wetting properties and water films on hydrophilic surfaces. *The J. Chem. Phys.* **146**, 164705 (2017).
43. D Turnbull, Kinetics of heterogeneous nucleation. *J. Chem. Phys.* **18**, 198–203 (1950).
44. M Kanduć, E Schneck, RR Netz, Attraction between hydrated hydrophilic surfaces. *Chem. Phys. Lett.* **610**, 375–380 (2014).
45. NB Rego, AJ Patel, Understanding hydrophobic effects: Insights from water density fluctuations. *Annu. Rev. Condens. Matter Phys.* **13**, 303 (2022).
46. I Siretanu, D van den Ende, F Mugele, Atomic structure and surface defects at mineral-water interfaces probed by in situ atomic force microscopy. *Nanoscale* **8**, 8220–8227 (2016).
47. EA Vogler, Structure and reactivity of water at biomaterial surfaces. *Adv. Colloid Interface Sci.* **74**, 69–117 (1998).
48. A Rosenhahn, S Schilp, HJ Kreuzer, M Grunze, The role of "inert" surface chemistry in marine biofouling prevention. *Phys. Chem. Chem. Phys.* **12**, 4275–4286 (2010).
49. M Kanduć, E Schneck, RR Netz, Understanding the "berg limit": the 65° contact angle as the universal adhesion threshold of biomatter. *Phys. Chem. Chem. Phys.* **26**, 713–723 (2024).
50. M Šako, F Staniscia, E Schneck, RR Netz, M Kanduć, Conditions for the stable adsorption of lipid monolayers to solid surfaces. *PNAS Nexus* **2**, pgad190 (2023).
51. C Oostenbrink, A Villa, AE Mark, WFV Gunsteren, A biomolecular force field based on the free enthalpy of hydration and solvation: The GROMOS force-field parameter sets 53A5 and 53A6. *J. Comput. Chem.* **25**, 1656–1676 (2004).
52. HJC Berendsen, JR Grigera, TP Straatsma, The missing term in effective pair potentials. *J. Phys. Chem.* **91**, 6269–6271 (1987).
53. MJ Abraham, et al., GROMACS: High performance molecular simulations through multi-level parallelism from laptops to supercomputers. *SoftwareX* **1–2**, 19–25 (2015).
54. G Bussi, D Donadio, M Parrinello, Canonical sampling through velocity rescaling. *The J. Chem. Phys.* **126**, 014101 (2007).

# PNAS



arXiv:2410.17626v1 [cond-mat.soft] 23 Oct 2024

## Supporting Information for

**Water cavitation results from the kinetic competition of bulk, surface and surface-defect nucleation events**

Philip Loche, Matej Kanduč, Emanuel Schneck and Roland R. Netz

Corresponding Author Matej Kanduč.  
E-mail: [matej.kanduc@ijs.si](mailto:matej.kanduc@ijs.si)

### This PDF file includes:

Figs. S1 to S3  
SI References

### S1. Fitting $\kappa_{2D}(\theta)$

To fit the data for  $\kappa_{2D}(\theta)$  in Fig. 2D in the main text, we use the following fitting function,

$$\kappa_{2D}(\theta) = \kappa_{2D,0} \exp \left[ \sum_{p=1}^4 (\theta/\theta_p)^p \right]. \quad [S1]$$

The fit yields  $\kappa_{2D,0} = 1.93 \times 10^{-35} \text{ ns}^{-1} \text{ nm}^{-2}$ ,  $\theta_1 = 0.21^\circ$ ,  $\theta_2 = 3.70^\circ$ ,  $\theta_3 = 12.61^\circ$ , and  $\theta_4 = 29.77^\circ$ . The resulting fit is shown as a solid line in Figs. 2D and S1A and was used in the subsequent analysis in the main text.

We also examine the implications of using a fitting function with a quadratic polynomial in the exponent for the subsequent analysis, given by

$$\kappa_{2D}(\theta) = \kappa_{2D,0} \exp \left[ \sum_{p=1}^2 (\theta/\theta_p)^p \right]. \quad [S2]$$

This fit, plotted as a dashed gray line in Fig. S1A does not match the data as well as the fourth-order polynomial fit. More critically, when we compute the resulting crossover contact angle  $\theta^*$  (using Eq. 11), shown in Fig. S1B, this quadratic fit predicts  $\theta^*$  below  $45^\circ$  for small box sizes  $L$ . This result is in contradiction with the simulation outcome for a contact angle of  $45^\circ$ , where homogeneous cavitation in the water phase occurs. Therefore, a fit limited to the second order does not adequately extrapolate to small contact angles.

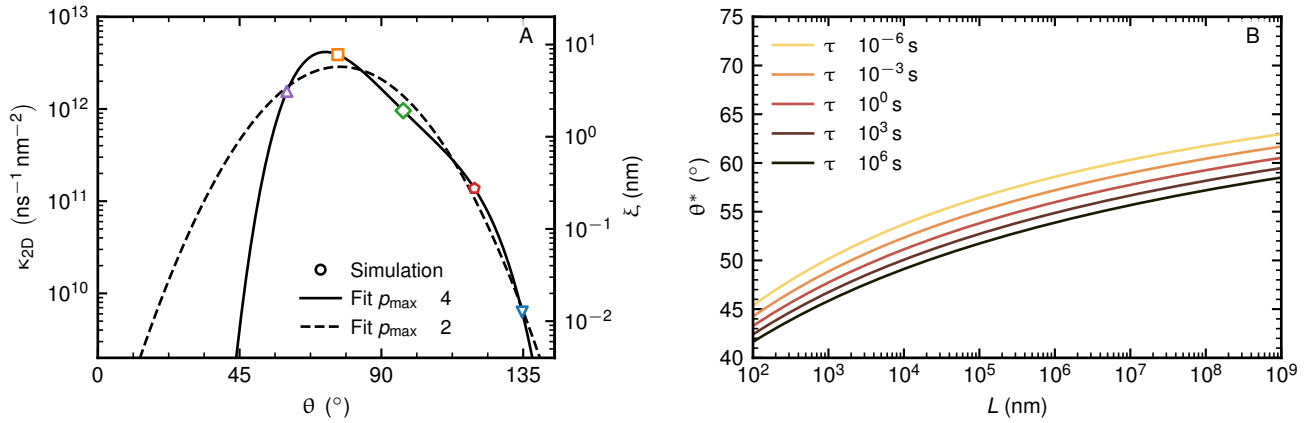


**Fig. S1.** (A) Fit of Eq. S1 (solid line, as in Fig. 2D in the main text) and Eq. S2 (dashed line) to the  $\kappa_{2D}$  data points from simulations. (B) Crossover contact angle  $\theta^*$  as a function of container size  $L$  for different waiting times  $\tau$ . Similar to Fig. 3B, but here based on the fit of Eq. S2 in Eq. 11.

### S2. Cavitation pressure for various waiting times $\tau$

In Fig. S2, we present the cavitation pressure as a function of contact angle, similar to Fig. 3A in the main text, but for considerably shorter (Fig. S2 A) and longer (Fig. S2 B) waiting times. We find that increasing  $\tau$  leads to a less negative cavitation pressure  $p_{\text{cav}}$  and a lower crossover contact angle  $\theta^*$  at which the cavitation transits from homogeneous to heterogeneous. The latter trend is also quantified in Fig. 3B.

### S3. Analytic estimate for crossover contact angle $\theta^*$

We derive an approximate expression for the crossover contact angle  $\theta^*$ , which follows from Eq. 11 in the main text. Taking the logarithm of both sides of Eq. 11 gives

$$\ln L = \frac{1}{3h(\theta^*) - 2} [\ln(6\kappa_{2D}\tau) - h(\theta^*) \ln(\kappa_{3D}\tau)] \quad [S3]$$

from which  $h(\theta^*)$  follows as

$$h(\theta^*) = \frac{\ln(6\kappa_{2D}L^2\tau)}{\ln(\kappa_{3D}L^3\tau)}. \quad [S4]$$

By expressing  $\kappa_{2D}$  in terms of  $\xi = \kappa_{2D}/\kappa_{3D}$ , we obtain

$$h(\theta^*) = 1 + \frac{\ln(6\xi/L)}{\ln(\kappa_{3D}L^3\tau)}. \quad [S5]$$

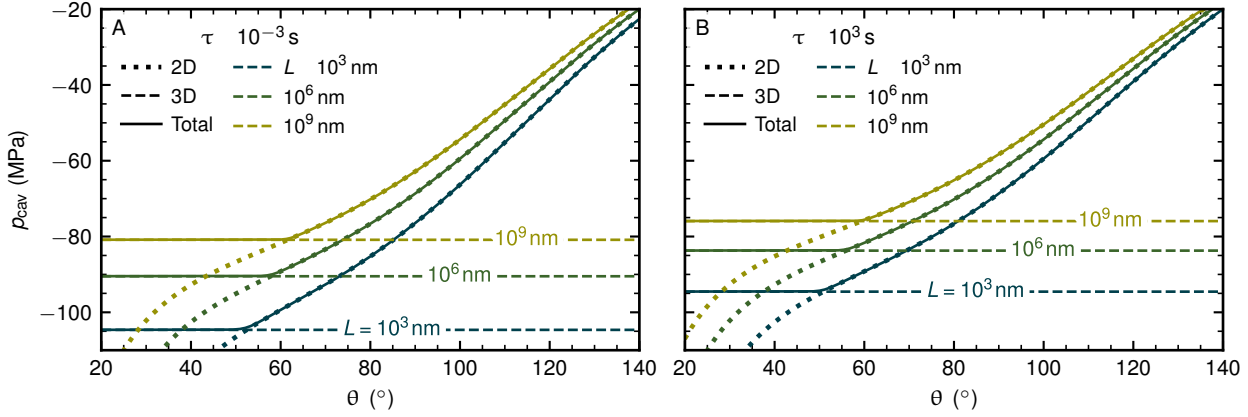


**Fig. S2.** Cavitation pressure  $p_{\text{cav}}$  as a function of contact angle  $\theta$ , similar to Fig. 3A in the main text, here shown for waiting times of (A)  $\tau = 1 \text{ ms}$  and (B)  $\tau = 1000 \text{ s} \approx 17 \text{ min}$ .

Next, we perform a Taylor expansion of the geometric function  $h(\theta^*)$ , given by Eq. 8, for small angles, which approximates as  $h(\theta) \simeq 1 - \frac{3}{16}\theta^4$ . Substituting this into Eq. S5 leads to the final expression

$$\theta^* \approx \left\{ \frac{16 \ln[(L/(6\xi))]}{3 \ln(\kappa_{3D} L^3 \tau)} \right\}^{1/4}, \quad [\text{S6}]$$

which is Eq. 12 in the main text.

#### S4. Relation between surface polarity $\alpha$ and contact angle $\theta$

The used model surface, resembling SAMs with tunable partial charges in the hydroxyl groups, has been thoroughly studied elsewhere (1). Fig. S3 shows the contact angle  $\theta$  as a function of the scaling factor  $\alpha$  of the hydroxyl group's partial charges. For  $\alpha = 0$  (i.e., the partial charges of the hydroxyl groups are 0), the surface is nonpolar, resulting in a contact angle of  $135^\circ$ . For  $\alpha > 0.86$ , the surface exhibit complete wetting, with  $\theta = 0$ . We fit the simulation data to

$$\cos \theta = c_0 + c_1 \alpha + c_2 \alpha^2 + c_3 \alpha^3, \quad [\text{S7}]$$

yielding the coefficients:  $c_0 = -0.70$ ,  $c_1 = -0.09$ ,  $c_2 = 0.65$ , and  $c_3 = 1.99$ . The fit is shown as a solid line in Fig. S3. This fit was used to determine the partial charges corresponding to a contact angle of  $\theta = 60^\circ$ , which had not been previously determined.

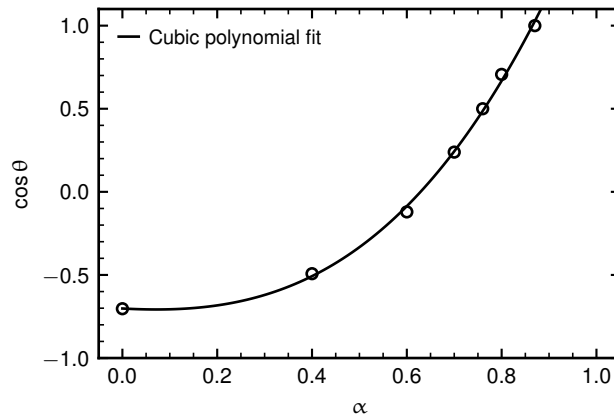


**Fig. S3.** Cosine of the contact angle  $\theta$  as a function of the SAM's surface polarity  $\alpha$ . Data is taken from Ref. 1. The solid line is the fit of Eq. S7 to the data points.

#### S5. Fitting the kinetic prefactor

Using classical nucleation theory, one can derive the free energy barriers as given by Eqs. 3 and 7. However, the kinetic prefactor is governed by various hydrodynamic and molecular effects, making it difficult to assess analytically. Atomistic simulations

provide a way to extract this factor. A straightforward approach might be to simulate a system at a specific pressure and track bubble formation. Unfortunately, this approach makes it challenging to observe cavity formation within practical simulation times, particularly without prior knowledge on the cavitation pressure. Therefore, we apply a time-dependent pressure ramp in the form

$$p(t) = \dot{p} t, \quad [\text{S8}]$$

to sample these rare events by solving time-dependent rate equations. Under this time-dependent pressure, the cavitation rate also becomes time-dependent and can be, in the Kramers framework, approximately expressed as

$$k(t) = k_0 e^{-\beta G^*(t)}. \quad [\text{S9}]$$

Note that for clarity we leave out the subscripts 3D or 2D since the equations are valid for both. The probability  $f(t)$  that the system has not yet crossed the barrier obeys a first-order rate equation

$$\dot{f}(t) = -k(t) f(t), \quad [\text{S10}]$$

with the formal solution

$$f(t) = e^{-k_0 I(t)}, \quad [\text{S11}]$$

where  $I(t)$  is given by

$$I(t) = \int_0^t e^{-\beta G^*(t')} dt'. \quad [\text{S12}]$$

In our pressure ramp simulations, the free energy barrier (given by Eqs. 3 or 7) decreases inversely with the square of time as

$$\beta \Delta G^*(t) = \left( \frac{\zeta}{t} \right)^2, \quad [\text{S13}]$$

with the time constants of the barrier  $\zeta$  for homogeneous (3D) and heterogeneous (2D) cavitation given by

$$(\zeta_{3\text{D}})^2 = \frac{16\pi}{3} \frac{\gamma^3}{\dot{p}^2}, \quad [\text{S14}]$$

$$\zeta_{2\text{D}} = \zeta_{3\text{D}} h(\theta). \quad [\text{S15}]$$

With the time-dependent free energy barrier given by Eq. S13, S12 has a closed-form solution

$$I(t) = t \exp \left[ - \left( \frac{\zeta}{t} \right)^2 \right] - \sqrt{\pi} \zeta \operatorname{erfc} \left( \frac{\zeta}{t} \right), \quad [\text{S16}]$$

where  $\operatorname{erfc}(x)$  is the complementary error function. The mean cavitation time in the pressure ramp protocol follows as

$$\tau = - \int_0^\infty t \dot{f}(t) dt = \int_0^\infty f(t) dt. \quad [\text{S17}]$$

Defining the dynamic cavitation pressure in the pressure ramp protocol as  $p_{\text{cav}}^* = \dot{p} \tau$ , one finds

$$p_{\text{cav}}^* = \dot{p} \int_0^\infty e^{-k_0 I(t)} dt. \quad [\text{S18}]$$

During a simulation, we apply a negative pressure rate  $\dot{p} < 0$  (i.e., the pressure is decreasing) and identify  $p_{\text{cav}}^*$ , the pressure at which cavitation occurs. Simulating several rates allows us to fit Eq. S18, where the kinetic prefactor  $k_0$  is the only fitting parameter.

## References

1. M Kanduč, RR Netz, Atomistic simulations of wetting properties and water films on hydrophilic surfaces. *The J. Chem. Phys.* **146**, 164705 (2017).